Supporting Information

Sub-Piconewton Force Detection Using Micron-Sized Wire Deflections

L. Chevry and J.-F. Berret*

Outline

S1 – **Characterization of nanoparticle sizes and size distribution**
S2 – **Vibrating sample magnetometry**
S3 – **Desalting transition: towards the fabrication of nanostructured wires**
S4 – **The bending profiles obey scaling laws**
S5 – **Bending profiles**
S6 – **Movie of a bending wire submitted to a rotating magnetic field**

S1 – Characterization of nanoparticle sizes and size distribution

Electron beam microdiffraction experiments were performed on the iron oxide dispersion using a Jeol-100 CX transmission electron microscope at the SIARE facility of University Pierre et Marie Curie (Université Paris 6). The electron beam was focused on a selected area comprising a large number of nanoparticles, which diffraction pattern was recorded in the Fourier plane of the microscope. The reinforcement of the scattering along the rings is interpreted as arising from the diffraction by nanoparticles of different orientations with respect to the incoming beam. The wave-vector dependence of the intensity is shown in Fig. S1. The high crystallinity of the nanoparticles was evidenced by the observation of Bragg reflections that were indexed thanks to a calibration with gold and attributed to maghemite iron oxide (γ-Fe_2O_3). Table S-I provides the list of the Bragg wave-vectors and Miller indices for γ-Fe_2O_3. The positions of the Bragg peaks found experimentally for maghemite nanoparticles compare well with those predicted for this structure.
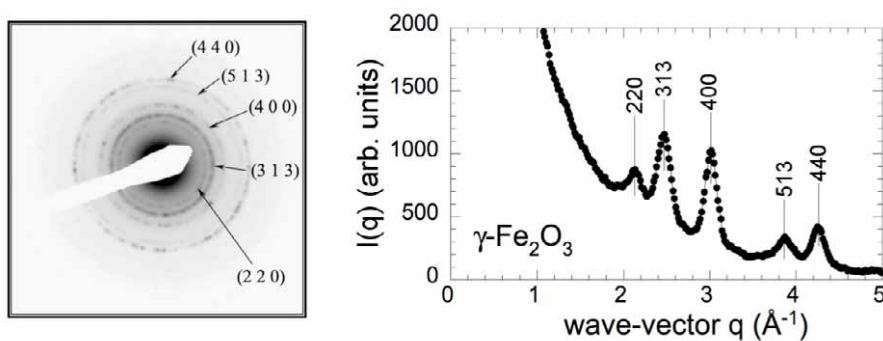

Figure S1*: Microdiffraction spectrum obtained for iron oxide nanoparticles (left). Wave-vector dependence of the scattering intensity obtained for iron oxide nanoparticles (right).*

1

Theoretical values and proportions for γ-Fe$_2$O$_3$			Experimental data
Miller indices for maghemite structure	q_i (Å^{-1})	Proportions	q_i (Å^{-1})
(2 2 0)	2.1299	30 %	2.13
(3 1 3)	2.5033	100 %	2.47
(4 0 0)	3.0063	15 %	3.01
(4 2 6)	3.6960	9 %	n.d
(5 1 3)	3.9270	20 %	3.86
(4 4 0)	4.2743	40 %	4.26

Table S-I : *Theoretical Miller indices, Bragg wave-vectors and proportions for maghemite structure, and experimental wave-vectors for the peaks observed in Fig. S1. The theoretical data are from R.M. Cornell, U. chwertmann, 1996, The iron oxides structure, properties, reactions, occurrences and uses, V.C.H., Weinheim. See also Dutta, P.; Manivannan, A.; Seehra, M. S.; Shah, N.; Huffman, G. P. Phys. Rev. B **2004**, 70, 174424, and references therein.*

S2 – Vibrating sample magnetometry (VSM)

Vibrating sample magnetometry (VSM) consisted in measuring the magnetization *versus* excitation M(H) for a solution at volume fraction ϕ from the signal induced in detection coils when the sample is moved periodically in an applied magnetic field (thanks to synchronous detection and with an appropriate calibration). Here we used the superparamagnetic nanoparticles having dominant populations at 8.3 nm. Fig. S2 shows the evolution of the macroscopic magnetization $M(H)$ normalized by its saturation value M_S for the γ–Fe$_2$O$_3$ superparamagnetic nanoparticles. Here, $M_S = \phi m_S$, where m_S is the specific magnetization of colloidal maghemite ($m_S = 3.5 \times 10^5$ A m^{-1}) and ϕ the volume fraction. The solid lines in Fig. S2 were obtained using the Langevin function for superparamagnetism convoluted with a log-normal distribution function of the particle size. The parameters of the distribution are the median diameter $D_0^{VSM} = 6.7$, 8.3 nm and 10.7 nm and the polydispersity $s^{VSM} = 0.21$, 0.26 and 0.33, respectively. These values are in relative good agreement with the ones obtained by TEM, albeit from a minor difference in diameter which could originate from defects located close to the surface and that would not contribute to magnetic properties.
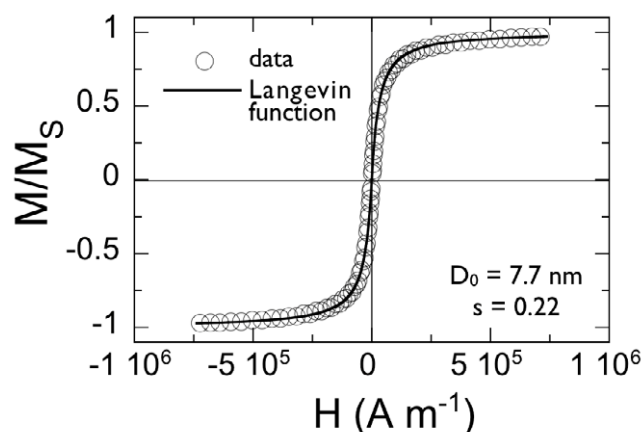

Figure S2: *Magnetic field dependence of the macroscopic magnetization M(H) normalized by its saturation value M_S for cationic maghemite dispersions. The solid curve was obtained using the Langevin function for superparamagnetism convoluted with a log-normal distribution function for the particle sizes, given with median diameters D_0^{VSM} and polydispersity s^{VSM}.*

S3 – Desalting transition: towards the fabrication of nanostructured wires

The protocols for mixing oppositely charged species described in this section were inspired by molecular biology and were developed for the *in vitro* reconstitutions of chromatin. The protocols applied here consisted first in the screening of the electrostatic interactions by bringing the dispersions of oppositely charged species to high salt concentration, and second in removing the salt progressively by *dialysis* or by *dilution*. With this technique, the oppositely charged species were intimately mixed in solution but did not interact owing to the electrostatic screening.

The *dialysis* or *dilution* strategies involved in a first step the preparation of separate 1 M salted solutions containing respectively the anionic particles and the cationic-neutral diblock copolymers. In order to improve their stability, the γ-Fe_2O_3 particles were coated by poly(acrylic acid) with molecular weight 2000 g mol^{-1} instead of citrate ligands as in the previous section.[30, 32] The thickness of the PAA_{2K} brush tethered on the surface was estimated at 3 nm by dynamical light scattering. The salt used in the present work was ammonium chloride (NH_4Cl). The two solutions were then mixed with each other and it was verified by light scattering that the colloidal stability was not altered by the excess of salt. In a second step, the ionic strength of the dispersions was progressively diminished, by *dialysis* or by *dilution*. Dialysis was performed against deionized water using a Slide-a-Lyzer$^{®}$ cassette with molecular weight cut-off 10000 g mol^{-1} (Fig. S3). The time evolution of the ionic strength was monitored by the measurement of the electric conductivity of the bath. Dialysis was carried under two different conditions, with or without magnetic field. The cartoon in Fig. 10 represents the case where the magnetic field (0.1 T) was on.[28] In the dilution process, deionized water was added stepwise to the nanoparticle and polymer salted dispersion, at a flow rate that was later translated into a desalting rate dI_S/dt, where I_S denotes the ionic strength. With dilution, it was possible to vary dI_S/dt from 10^{-5} to 1 M s^{-1}. With dialysis, the average rate of ionic strength change was of the order of 10^{-3} - 10^{-4} M s^{-1} and the particle concentration remained practically constant.
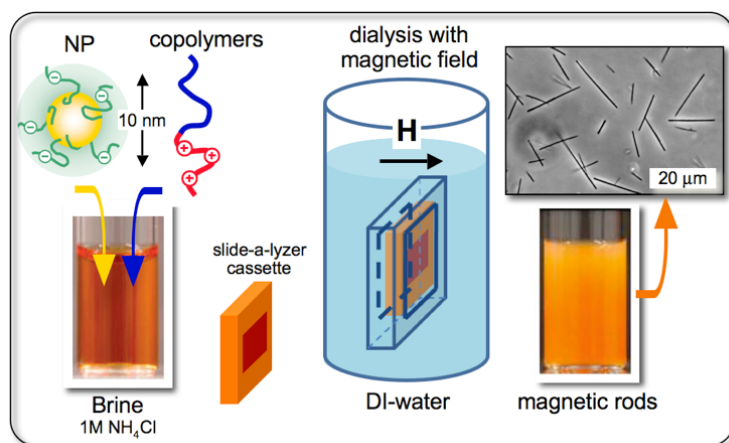

Figure S3: *Schematic representation of the protocol that controls the nanoparticle co-assembly and wire formation.*[22]

S4 – The bending profiles obey scaling laws

As mentioned in the main text, the bending profiles of the wires, noted $y(x)$ were obtained from the digitalization of the images, and fitted using scaling laws of the form $y \sim x^{\alpha}$, where α was an adjustable parameter. Interestingly, the exponents of the scaling were around 2 at low deflections, that

is for angle $\beta < 45°$ and for magnetic field $B < 6\,mT$. Above these limits, the value of the exponent rose up to 3. The variations of the exponent as a function of the orientation angle and of the magnetic field are illustrated in Figs. S4a and S4b respectively.
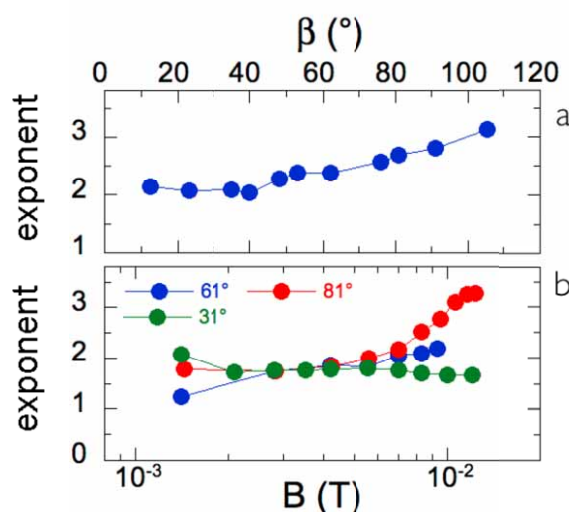

Figure S4: *Dependences of the scaling exponent α versus orientation angle (a) and magnetic field (b) for bent wires.*

S5 – Bending profiles

Fig. 6a in the main text show the magnetic field dependence of the quantity $8R_C\Delta\chi L \sin(2\beta)/\mu_0 D^2$. In this expression, R_C is the radius of curvature, $\Delta\chi = \chi^2/(2 + \chi)$ where χ is the magnetic susceptibility, L and D the length and diameter of the wire. These data were obtained from the $y(x)$-profiles shown for three configurations: *i)* $L = 96\ \mu m$ and $\beta = 31°$; *ii)* $L = 72\ \mu m$ and $\beta = 61°$, and *iii)* $L = 125\ \mu m$ and $\beta = 81°$.
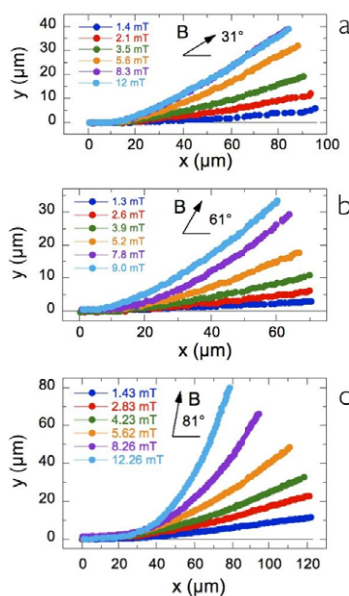

Figure S5: *Experimental $y(x)$-profiles obtained in three different configurations of wire and magnetic field orientations.*

S6 – Movie of a bending wire submitted to a rotating magnetic field

The movie can be uploaded from the journal website. Fig S6 illustrates the deflections of the wire at different times of the experiment.
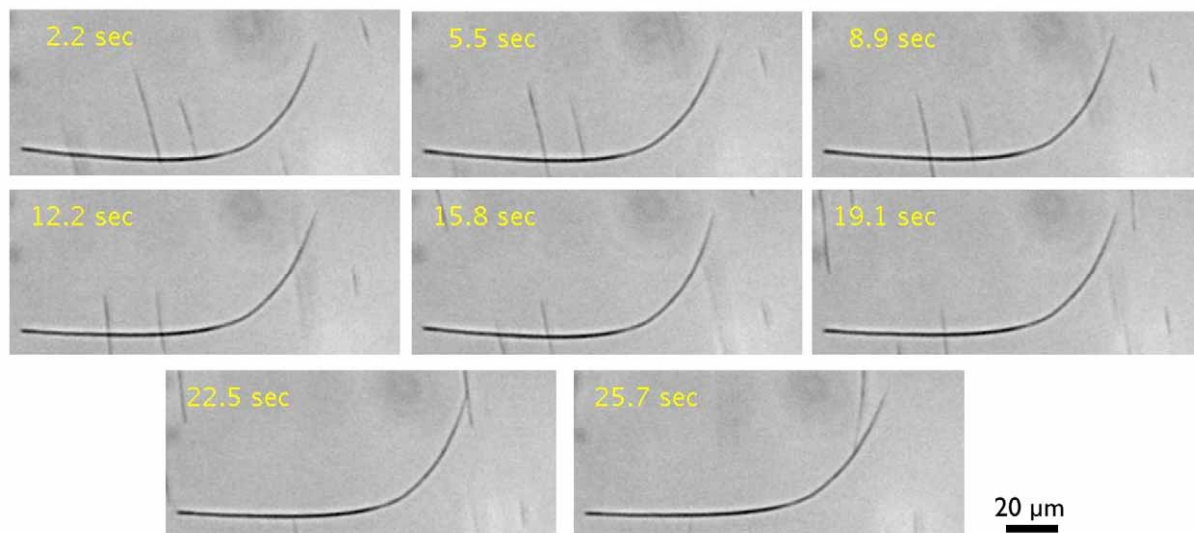

Figure S6: Wire submitted to a rotating magnetic field.